Atomic-scale Investigation of $Na_3V_2(PO_4)_3$ Formation Process in Chemical Infiltration via *In situ* Transmission Electron Microscope for Solid-State Sodium Batteries

Tzu-Hsuan Yu [a], *Chih-Yang Huang* [a], *Min-Ci Wu* [a], *Yen-Jung Chen* [a], *Lan Tu*[b,c], *Chih-Long Tsai* [b], *Jeng-Kuei Chang* [a], *Rüdiger-A. Eichel*[b,d] *and Wen-Wei Wu* [a,e,f,*]

[a] Department of Materials Science and Engineering, National Chiao Tung University, Hsinchu, 30010, Taiwan

[b] Forschungszentrum Jülich GmbH, Institute of Energy and Climate Research, 52425 Jülich, Germany

[c] Empa, Swiss Federal Laboratories for Materials Science and chnology, Überlandstrasse 129, 8600 Dübendorf, Switzerland

[d] Institut für Materialien und Prozesse für elektrochemische Energiespeicher– und wandler, RWTH Aachen University, 52074 Aachen, Germany

[e] Center for the Intelligent Semiconductor Nano-system Technology Research, Hsinchu, 30078, Taiwan

[f] Frontier Research Center on Fundamental and Applied Sciences of Matters, National Tsing Hua University, Hsinchu, 30013, Taiwan

* Corresponding author:
wwwu@mail.nctu.edu.tw (Wen-Wei Wu)

Abstract

Ceramic-based all-solid-state sodium batteries (Na-ASSBs) are prospective alternative energy storage systems due to the abundant sodium resources and their high safety. A previous study showed that chemical infiltration could methodically improve not only the contact between the positive electrode ($Na_3V_2(PO_4)_3$) (NVP) and solid electrolyte ($Na_{3.4}Zr_2Si_{2.4}P_{0.6}O_{12}$) (NZSP) but also the electrochemcial performance of the battery. However, detailed information on the corresponding structural evolution remains lacking. In this work, the synthesis process of NVP on NZSP substrate was first investigated at the atomic scale by *in situ* high-resolution transmission electron microscope (HRTEM) and energy dispersive spectroscopy (EDS). The entire calcination process consisted of crystallization and aggregation of NH_4VO_3 and NaH_2PO_4 precursors, and then formation of NVP. During the formation process, NaH_2PO_4 diffused into NVP because of its light atomic weight. In contrast, NH_4VO_3 maintained its position instead of diffusing. Furthermore, HRTEM movies and the corresponding fast fourier transforms (FFTs) pattern demonstrated that NVP epitaxially grew with NH_4VO_3 and NaH_2PO_4. This study first reveals the formation and growth processes of NVP at the atomic scale. These results provide not only fundamental information but also a basis for further development of Na-SSSBs.

Key words: *In situ* HRTEM, Solid-state sodium batteries, Calcination, Epitaxial growth, $Na_3V_2(PO_4)_3$ (NVP)

1. Introduction

Energy issues are undoubtedly one of the most critical problems of this century. With the increasing demand for energy, scientists are committed to research more environmentally friendly and low-cost alternative energy storage systems[1, 2]. In recent years, sodium-ion batteries (SIBs) have become promising options owing to the ubiquitous sodium resources and lower environmental impact than lithium-ion batteries (LIBs). However, the energy density and cyclability of conventional SIBs with liquid electrolytes remain imperfect. Therefore, some studies have been extended to developing various SIBs with different types of electrodes/electrolytes to improve the performance and explore the applications[3].

Among these Na based energy storage systems, ceramic-based all-solid-state sodium batteries (Na-ASSBs) are a promising choices with their higher energy density and safety when compared to SIBs[4]. However, the contact problem between the positive electrode and solid electrolyte often caused the conductivity and cyclability properties of the battery to be unsatisfactory[5]. Since the contacts of conventional co-sintered interfaces are rigid, volume changes of electrode active material while cycling would damage the interface, which results in ceramic-based Na-ASSBs to degrade after a few cycles. Recently, methods such as using composite polymer layers or thin film electrodes were reported to solve these problems[6-8]. Even so, these methods still have disadvantages. For example, a higher operation temperature is required for composite polymer electrolytes due to the much lower Na-ion conductivity of polymer conductor,

and thin film cathodes are not suitable for large-scale applications, especially when a high energy density is required [6-8].

To solve the problem mentioned above, chemical infiltration was invented. Chemical infiltration is a method that combines *in situ* synthesis and sintering[4]. A precursor solution of the positive electrode infiltrates in the solid electrolyte and forms a positive electrode on the solid electrolyte after the calcination process. $Na_3V_2(PO_4)_3$ (NVP) is a common electrode material in SIBs owing to its high capacity, high thermal and structural stability[2, 9, 10]. However, a low ionic conductivity due to the large radius of Na^+ is a limitation. To solve this problem, different architectures of NVP electrodes have been developed, such as carbon coating NVP electrodes[1], 3D porous sphere NVP/C[11, 12], N-doped NVP[13] and even layer-by-layer NVP embedded in graphene oxide[14]. However, the synthesis process is complex and difficult to achieve mass production[1, 11-14]. Applying chemical infiltration to the NVP/$Na_{3.4}Zr_2Si_{2.4}P_{0.6}O_{12}$ (NZSP) system not only enhanced the electrical conductivity of NVP due to the *in situ* formation of carbon surrounding but also resolved the contact problem of solid-state batteries (SSBs)[4]. The interface formed by this method effectively reduced the stress caused by volume changes during cycling. Therefore, a Na-ASSB with highly stable performance and lower internal resistance of about 570 Ω (396 Ω cm^2) under room temperature was reported, which was smaller than other typical solid-state batteries [4]. In fact, one of the reasons that can improve the properties of Na-ASSBs is because the structures of NVP and NZSP are both sodium

super ionic conductor (NASICON). NASICON structure materials generally perform high energy density and structure stability since their 3-dimensional (3D) open framework[15]. NVP and NZSP are both NASICON with the space group of $R\bar{3}c$. By combining them, the battery with high intrinsic energy density, high thermal and electrochemical stability could be developed. These properties were strongly related to the synthesis conditions of NVP, which might result from the microstructures. However, details of microstructure evolution during calcinating remain lacking. Hence, investigation of the fundamental mechanism of NVP growth is essential. Nevertheless, most researches only utilized X-ray diffraction (XRD), which could not provide high-spatial-resolution information of the calcination process[16-18]. Therefore, developing new techniques for better resolution is urgently needed.

In situ transmission electron microscope (TEM) is one of the most powerful instruments that has been effectively used in a wide range of applications, such as magnetic devices, optical devices and batteries[19-23]. The greatest advantage of this technique is that it can reveal dynamic microstructure evolution and atomic behavior in real time [24-27].The calcination process of ceramic-based Na-ASSBs was first investigated in this study. The complete formation of NVP while calcinating was observed at the atomic scale using *in situ* TEM. The aggregation process of precursors, namely NaH_2PO_4 and NH_4VO_3, and epitaxial growth of the precursors with NVP were clearly observed. The results provided an in-depth understanding of the fundamental science of electrode materials, which can be applied to improving the performance and

exploring the development of Na-ASSBs.

2. Results and Discussion

Fig. S1 shows the cross -section of the pristine NVP precursors/NZSP pellets. The STEM image (Fig. S1a) brings an obvious difference between the NVP precursors and NZSP. The enlarged TEM image and the corresponding FFT show that the precursors were amorphous (Fig. S1b). On the other hand, NZSP was crystalline and highly compacted leading to a brighter contrast than that of the NVP precursor layer (Fig. S1c). According to the energy dispersive spectroscopy (EDS) mapping analysis, the distribution of V, Zr and Si also made certain NVP precursors and NZSP (Fig. S1d-f). Although the Si signal was interfered by the SiN_x membrane on the *in situ* TEM heating chip, the distribution of the Si signal at NZSP still had a stronger contrast.

Observing the calcination process by *in situ* TEM can provide information on the conversion behavior. All reactions in this study were operated at 700 ℃. *In situ* TEM at low magnification mainly provided the information of overall conversion behaviors. The complete NVP calcination process from a macroscopic perspective is presented in Movie S1 and consisted of an aggregation process and growth process. The series of TEM images show that the reactant particles aggregated to form larger particles; then, some of the particles merged in the left particle and others attached to the surface of NZSP (Fig. 1a-d). Afterwards, growth occurred after aggregation (Fig. 1e-h). It is worth mentioning that particles trimmed the boundary and displayed a sharp surface during

growth (Fig. 1i-l). The more obvious boundary-trimming phenomenon was investigated under higher magnification (Movie S2 and Fig. S2). The details of the NVP growth process require investigation at higher resolution and will be provided in the following paragraphs. According to the high-resolution transmission electron microscope (HRTEM) image and EDS mapping analysis, the particle in the upper corner after the calcination process was identified as NVP (Fig. 1m-r), as was the particle on the right side of the frame area (Fig. 1s). Based on the flat surface observed above, it could be concluded that the thermodynamic driving force for NVP formation in this study was energetically favorable[28]. In addition, electron energy loss spectroscopy (EELS) was also utilized to investigate the valence state of the V element (Fig. 1t). The split peaks at the shoulder of V-L_3 edge with the valence state of +5 appear when energy resolution increased[29]. Nevertheless, peak shift of O-K edge occur when large amount of defects exist[30], which might cause the overlap of V-L_2 edge and O-K edge. As attested by the EELS spectra, the *L*-edge chemical shift indicated the valence change of V. The valence state of V transformed from +5 to +3, which coincided with the valence state change of V ions from precursor NH_4VO_3 to NVP[31-33].

To reveal detailed information on the calcination process, *in situ* HRTEM experiments must be performed for a deeper understanding of fundamental science. The following atomic-scale discussion was divided into the aggregation process of precursors and the growth process of NVP. Movie S3 shows that all of the NVP precursors were nearly amorphous in the initial state. The TEM image and the

corresponding fast fourier transform (FFT) pattern in Fig. S3a indicate precursors with a non-crystalline diffraction pattern. With increasing heating time, amorphous precursors gradually crystallized. As the heat was continuously applied, the number of polycrystalline rings of FFTs increased, indicating that the crystallinity of the precursors increased (Fig. S3b-f). Afterwards, an increasing number of particles can be discovered in Movie S3 (Fig. S3g-j). Only two types of NVP precursors, NaH_2PO_4 and NH_4VO_3, could be crystalline[34-36], and the formation energy are -2.196 eV/atom[37] and -1.429 eV/atom[38], respectively. Therefore, they were the focus of the aggregation process of the precursors, which was demonstrated in Movie S4. In Movie S4, two particles with different contrast could be recognized. According to the HRTEM image and the corresponding FFTs of non-overlapping phases, the particles were identified as NaH_2PO_4 and NH_4VO_3, respectively. (Fig. 2a-c). NH_4VO_3 initially aggregated inward when heated (Fig. 2d-e), followed by NH_4VO_3 aggregating with NaH_2PO_4 within a short time period. Here we infer that the final product would be NVP. In addition, schematic illustrations of the aggregation process of the precursors are shown in Fig. 2g-j. Moreover, individual coalescence phenomena of NH_4VO_3 and NaH_2PO_4 were also recorded in Movies S5 and S6. The coalescing processes of NH_4VO_3 and NaH_2PO_4 are shown in Fig. S4 and Fig. S5.

According to the TEM images at low magnification, the NVP growth process was followed by the aggregation of precursors. Therefore, the detailed growth process of NVP was investigated here via HRTEM after the aggregation of precursors was

revealed. Notably, the unique epitaxial growth behavior of NVP was demonstrated for the first time, which was with NH_4VO_3 (Movie S7) and NaH_2PO_4 (Movie S8), respectively. The series of TEM images (Fig. 3) shows the details of NVP epitaxial growth with NH_4VO_3. Initially, NH_4VO_3 had flat surfaces of (100) and $(0\bar{1}1)$. NH_4VO_3 started shrinking at 6 s and adjusted the planes to (100) and $(\bar{1}21)$. NH_4VO_3 with orthorhombic structure display a low surface energy with (100) facets[39], leading to sharp surface of $(100)_{NH4VO3}$ at the zone axis of [011] and [012]. After adjusted the planes, the surface energy of $(1\bar{2}1)_{NH4VO3}$ is large, leading to the morphology is not flat. Therefore, NH_4VO_3 looked not as flat as NVP. Afterwards, NVP grew from the right side at 9 s, as highlighted by red dashed lines, and NH_4VO_3 eventually became NVP (Fig. 3 and Fig. 4a-b). It could be observed that NH_4VO_3 maintained its original position, and NVP was formed at the interface. A previous study demonstrated that the degree of order was low at the boundaries, leading to lower energy consumption during diffusion[27]. In addition, NaH_2PO_4 was liable to diffuse owing to all elements in NaH_2PO_4 were light. Therefore, we assumed that NaH_2PO_4 diffused through the boundary. Afterwards, NaH_2PO_4 combined with NH_4VO_3 to formed NVP when stoichiometry was achieved. Based on the results of the HRTEM image and the corresponding FFT at 14 s, epitaxial relationships could be identified as $[012]_{NH4VO3}//[12\bar{1}]_{NVP}$ and $(12\bar{1})_{NH4VO3}//(2\bar{1}0)_{NVP}$[40]. The distance of $(100)_{NH4VO3}$ conformed to 0.491 nm and that of $(202)_{NVP}$ conformed to 0.357 nm in the HRTEM image (Fig. 4b). Since the lattice mismatch of $(12\bar{1})_{NH4VO3}$ and $(2\bar{1}0)_{NVP}$ was about 30%,

it should be modified by a 3-to-2 epitaxial relationship. The modified lattice mismatch could be calculated by: $\delta = md_{sub} - nd_{epi}/md_{sub}$, where δ is the lattice mismatch, d is the d-spacing, m and n are the multiple factors[41]. The theoretical lattice mismatch δ in our system was approximately 8.1%. Base on the experimental value, the strain of NVP was 5% and that of NH_4VO_3 was evaluated to be 6.6%. To better understand the process, enlarged HRTEM images and FFT filtered images at the boundary of NH_4VO_3 and NVP are shown in Fig. 4c. The NH_4VO_3 lattice was filtered on the FFT in blue, and the NVP lattice was filtered in red. It could be observed that NVP grew along the epitaxial plane of (202), which transformed NH_4VO_3 into NVP. The positional relationship of V atoms in NH_4VO_3 and NVP is shown in Fig. 4d. Blue balls represent the position of V atoms in NH_4VO_3, and red balls represent that in NVP. We assumed NVP epitaxially growing along (202) with NH_4VO_3 because of the similar atomic positions of V in their atomic structures. That is, the reaction required only NaH_2PO_4 to diffuse and achieve stoichiometry from the boundary, which consumed less energy. Consequently, the atomic behaviors between NVP and NH_4VO_3 were investigated.

On the other hand, the epitaxial growth process of NVP with another precursor, NaH_2PO_4, is shown in Movie S8 and Fig. 5. The series of TEM images show that NaH_2PO_4 aggregated inward and then diffused into NVP. The area of the final product increased while NaH_2PO_4 diffused inside (Fig. 5a-e). The area of as-formed NVP decreased as shown in Fig. 5f, which resulted from that NVP adjusted the morphology to decrease the surface energy. This behavior confirmed our above inference that

NaH_2PO_4 diffused into NVP rather than NVP grew along with NaH_2PO_4. The HRTEM image and the corresponding FFT at 13 s reveal the orientation relationships of NaH_2PO_4 and NVP as $[\bar{3}21]_{NaH2PO4}//[210]_{NVP}$ and $(\overline{12}1)_{NaH2PO4}//(009)_{NVP}$[40]. The d-spacing of $(111)_{NaH2PO4}$ matched 0.457 nm[42] and that of $(\bar{1}2\bar{3})_{NVP}$ matched 0.347 nm[4] (Fig. 5g). For a deeper discussion of the diffusion process, enlarged HRTEM images at the boundary of NaH_2PO_4 and NVP are shown in Fig. 5 h-i. Because of the problem of projection under TEM observation, the direction of NaH_2PO_4 diffusion (the orange arrow) could not be recognized from the diffraction pattern[27]. The diffusional direction was always related to the direction with the highest atomic density on its closest packing surface, which needed the lowest energy for diffusion, and that in the monoclinic structure was reported to be {110}[43]. Therefore, we speculated that NaH_2PO_4 diffused along the [110] direction. Before all NaH_2PO_4 diffused into NVP, NaH_2PO_4 exposed the (111) surface, which was an energetically favorable surface for NaH_2PO_4 (Fig. 5j). A schematic illustration at the interface of NaH_2PO_4 and NVP is shown in Fig. 5k. Lattice points were applied as demonstrations due to the structure of NaH_2PO_4 was complicated. The definition of lattice points in NaH_2PO_4 (Fig. S6) was as follows. First, the atom positions of O and Na elements were exported from CrystalMaker software (Fig. S6a). Second, figured out the pattern of atomic arrangement and determined green circles as lattice points of NaH_2PO_4 (Fig. S6b). Third, green balls were defined at the positions of lattice points (Fig. S6c). Finally, the positions of green balls were not only arranged regularly but also fitted the results of

the NaH_2PO_4 HRTEM image in Fig. 5g (Fig. S6d). Based on the HRTEM results mentioned above, the precursors transformed into NVP without forming intermediate phases and the detailed atomic conversion behaviors of NVP epitaxially growth with NH_4VO_3 and NaH_2PO_4 were observed and systematically analyzed as the description below. At 700℃, NVP would form at the boundary of NH_4VO_3 and NaH_2PO_4. As the observed results in Figure 4 and Figure 5, NaH_2PO_4 diffused into NH_4VO_3 during the growth process of NVP. NH_4VO_3 maintained its original position and transformed into NVP when the diffused NaH_2PO_4 achieved the stoichiometric amount. According to the epitaxial relationship between NH_4VO_3 and NVP, the atomic positions of V were almost overlapped, indicating that V didn't obviously diffuse during the growth process. On the other hands, the elements in NaH_2PO_4 continuously diffused toward the NH_4VO_3/NVP interface until the end of NVP growth.

To reveal the actual driving force, the experiment operated below critical temperature (< 700℃) is shown in Movie S9 and Fig. S7. Precursors only increase in crystallinity without forming NVP while heating. In the beginning, precursors of NVP were amorphous. When the heating temperature was close to the critical temperature (~700℃), precursors of NVP started to crystallize and formed nanograins. At 700℃, precursors began to coalesce violently and became larger particles. When NH_4VO_3 and NaH_2PO_4 contacted each other, NVP formed, and then all reactants turned into the final product. Hence, we concluded that only the crystallinity of precursors increased below 700℃, and the formation of NVP only occurred at the temperature above 700℃.

Moreover, even under the same magnification as the previous movies (Movie S2-S8), if the temperature doesn't reach the critical temperature, NVP will never form. Therefore, the dominating driving force is the temperature.

To confirm that the results of *in situ* HRTEM match *ex situ* pellets, *ex situ* calcination specimens were investigated via XRD (Fig. S8) and TEM (Fig. S9) analyses. As shown in the XRD spectra of the pristine (NVP precursors/NZSP) pellet, only NZSP signals were detected. The diffraction peaks of NZSP were indexed to NASICON-type NZSP with the space group of $R\bar{3}c$[4]. The signals of NVP appeared in the calcined specimen, which were also indexed to the NASICON structured NVP with the space group of $R\bar{3}c$ (JCPDS No. 053–0018)[10]. The XRD results agreed with those of the *in situ* TEM experiment, proving that the final product was NVP (Fig. S8). The final product of the *ex situ* specimen could also be confirmed as NVP through the HRTEM image and its corresponding FFT (Fig. S9a). According to the scanning transmission electron microscope (STEM) image and EDS mapping analysis of V, Zr and Si elements, no interdiffusion or impurity phase was observed at the interface (Fig. S9b-e). In addition, some voids are shown in Fig. S9b at the interface of NVP and NZSP. The voids could accommodate the stress caused by the volume change during cycling and reduce damage to the interface[4]. Moreover, since the surface of NZSP was quite uneven, NZSP could be the attachment point for NVP while calcinating. Hence, fabricating NVP/NZSP pellets by a chemical infiltration method could methodically improve the interfacial structure and be helpful for increasing the ionic and electrical

conductivity of pellets.

With the complete NVP synthesis process revealed, the overall reaction mechanism is demonstrated in Fig. S10. At the initial stage, NH_4VO_3 and NaH_2PO_4 precursors were dispersive (Fig. S10a). As heat was continuously applied, precursors aggregated and clustered together (Fig. S10b-c). Afterwards, the same precursors coalesced and became larger nanoparticles. When NH_4VO_3 and NaH_2PO_4 contacted each other, NVP formed, and then all reactants turned into the final product (Fig. S10d-g). In addition, schematic illustrations of the atomic model for precursors with NVP are shown in Fig. S11. A deeper discussion of the NVP synthesis process at the atomic scale is provided in Fig. 6. The formation of NVP could be divided into three steps. First, the phase transformation of NH_4VO_3 and NaH_2PO_4 precursors from amorphous to crystalline structures occurred (Fig. 6a). Second, precursors aggregated together and formed NVP. As mentioned above, coalescence processes of NH_4VO_3 and NaH_2PO_4 and even aggregation behavior of NH_4VO_3 and NaH_2PO_4 were observed (Fig. 6b). Third, NVP epitaxially grew with the precursors. NVP grew along with NH_4VO_3 because the atomic positions of V in NVP were similar to those in NH_4VO_3. When NaH_2PO_4 accessed the boundary of NH_4VO_3 and NVP, it combined with NH_4VO_3 and transformed into NVP when stoichiometry was achieved. This transformation required lower energy owing to that NH_4VO_3 did not need to move too far to form the final product. On the other hand, NaH_2PO_4 tended to diffuse into NVP because of its light atomic weight. Therefore, compared with the growth process of NVP and NH_4VO_3, the

area of the final product increased after NaH_2PO_4 diffused into it (Fig. 6c). The complete synthesis process of NVP was revealed, and the mechanism was established at the atomic scale for the first time.

3. Conclusion

The complete calcination process of NVP from precursors was investigated at the atomic scale via *in situ* TEM. Interesting evolutionary behaviors of electrode material while heating were first observed. The NH_4VO_3 and NaH_2PO_4 precursors aggregated and formed NVP after the crystallization process. It is noteworthy that the individual epitaxial relationship and growth behaviors of NVP with NH_4VO_3 and NaH_2PO_4 were clearly observed and analyzed. Moreover, the formation of SIB cathode material was revealed for the first time, which opens up novel investigation methods for various electrode materials. This study not only provided detailed fundamental science information but also broadened the scope of electrode materials. Furthermore, an in-depth understanding of NVP could be applied to improve the performance and explore the development of Na-ASSBs.

4. Experimental Section

4.1 Preparation of pellets: Fabrication of NZSP powder was performed as follows. $NaNO_3$, $ZrO(NO_3)_2$, $Si(OCH_2CH_3)_4$, and $NH_4H_2PO_4$ were first dissolved in deionized H_2O. Then, the solution was dried at 85 °C and calcinated at 800 °C for 3 h, followed

by the powder being mixed with zirconia ball milling in ethanol for 48 h and then dried at 70 °C for 12 h. The mixed powder was pressed into pellets at 90 MPa and sintered in air at 1280 °C for 6 h to form NZSP pellets. On the other hand, an NVP precursor solution was prepared from ethanolamine, NaH_2PO_4, NH_4VO_3 and deionized H_2O. The as-synthesis solution was dropped on the surface of the NZSP pellet and infiltrated the NZSP layer. A schematic illustration of the NVP precursor/NZSP pellet is shown in Fig. S12a.

4.2 *In situ* TEM observation: An *in situ* TEM sample of pristine NVP precursors/NZSP pellet was produced via focus ion beam (FIB) (TESCAN LYRA3). Before lamella preparation, a layer of platinum protection was deposited by the FIB to avoid damage from Ga-ion milling. Notably, the deposition of the platinum protection layer was divided two times because of the uneven surface of the pellet (Fig. S12b-d). A Pt layer was deposited to fill the surface for the first time, and then the Pt layer was thickened to protect the sample for the second time. A low kV cleaning process was used to minimize the influence of Ga ions from the FIB at the end of lamella preparation. Moreover, the thickness of the specimen was controlled under 100 nm to meet the requirements for high-resolution images (Fig. S12e-f). The as-prepared TEM lamella specimen was transferred by a glass tip onto the *in situ* TEM heating chip. The *in situ* TEM system include Protochips fusion select holder (Audro 300) and tilt controller, power supply system (2616A System Sourcemeter) and software controller (Fusion 350 V1.0.0). The TEM lamella specimen was transferred by a glass tip onto the *in situ* TEM

heating chip. Subsequently, the chip was loaded onto the *in situ* TEM holder. We utilized the software controller to set the experimental parameters such as target temperature and heating rate. Besides, the tilt controller can control the y-axis of the stage for further HRTEM identification (Fig. S13). All *in situ* TEM movies and TEM images were taken via a JEOL-F200, and the element distribution was obtained by energy dispersive spectrometer (EDS) equipped with TEM.

4.3 Characterization of *ex situ* pellets: The as-prepared NVP precursor/NZSP pellet was calcined at 740 °C in Ar-4% H_2 for 4 h to form an *ex situ* NVP/NZSP pellet. XRD patterns of pristine and calcined pellets were measured by a Brucker D2 Phaser with Cu Kα radiation. The lamellar specimen of the *ex situ* pellet was produced by the abovementioned FIB in the same way. Afterwards, the lamellar specimen was transferred by a glass tip onto Cu grids to obtain *ex situ* sample information. The valence states of V element in precursors and as-calcined NVP were characterized using EELS combined with TEM (JEOL-F200).

Appendix A. Supplementary data

Supplementary data associated with this article can be found, in the online version, at https://doi.org/XXX.XXXXX/XXXXXXX.

Notes

The authors declare no competing financial interest.

Acknowledgements

The author W.-W.W. acknowledges the support from the Ministry of Science and Technology (MOST) in Taiwan (MOST 106-2628-E-009-002-MY3, MOST 106-2119-M-009-008, MOST 107-2119-M-009-019, MOST 108-2221-E-009-036-MY3, MOST 109-2628-E-009-008-MY3 and MOST 110-2731-M-009-001). This work was financially supported by the "Center for Semiconductor Technology Research of National Chiao Tung University" from The Featured Areas Research Center Program within the framework of the Higher Education Sprout Project by the Ministry of Education (MOE) in Taiwan. This work was also supported in part by the Ministry of Science and Technology, Taiwan, under Grant MOST-109-2634-F-009-029 and MOST-110-2634-F-009-027.

References

[1] X. Rui, W. Sun, C. Wu, Y. Yu, Q. Yan, Advanced Materials, 27 (2015) 6670-6676.
[2] Y. Jiang, X. Zhou, D. Li, X. Cheng, F. Liu, Y. Yu, Advanced Energy Materials, 8 (2018) 1800068.
[3] W. Zhang, C.-D. Zhao, X.-L. Wu, Advanced Materials Interfaces, 7 (2020) 2001444.
[4] T. Lan, C.-L. Tsai, F. Tietz, X.-K. Wei, M. Heggen, R.E. Dunin-Borkowski, R. Wang, Y. Xiao, Q. Ma, O. Guillon, Nano Energy, 65 (2019) 104040.
[5] Z. Zhang, Q. Zhang, J. Shi, Y.S. Chu, X. Yu, K. Xu, M. Ge, H. Yan, W. Li, L. Gu, Y.-S. Hu, H. Li, X.-Q. Yang, L. Chen, X. Huang, Advanced Energy Materials, 7 (2017) 1601196.
[6] W. Zhou, Y. Li, S. Xin, J.B. Goodenough, ACS Central Science, 3 (2017) 52-57.
[7] H. Gao, S. Xin, L. Xue, J.B. Goodenough, Chem, 4 (2018) 833-844.
[8] P. Kehne, C. Guhl, Q. Ma, F. Tietz, L. Alff, R. Hausbrand, P. Komissinskiy, Journal of The Electrochemical Society, 166 (2019) A5328-A5332.
[9] Q. Zeng, L. Luo, Z. Yu, L. Jiang, Solid State Ionics, 323 (2018) 92-96.
[10] K. Saravanan, C.W. Mason, A. Rudola, K.H. Wong, P. Balaya, Advanced Energy

Materials, 3 (2013) 444-450.
[11] J. Mao, C. Luo, T. Gao, X. Fan, C. Wang, Journal of Materials Chemistry A, 3 (2015) 10378-10385.
[12] T. Wei, G. Yang, C. Wang, Nano Energy, 39 (2017) 363-370.
[13] H. Zhang, I. Hasa, B. Qin, T. Diemant, D. Buchholz, J. Behm, S. Passerini, ChemElectroChem, 4 (2017) 1256-1263.
[14] Y. Xu, Q. Wei, C. Xu, Q. Li, Q. An, P. Zhang, J. Sheng, Z. Liang, L. Mai, Advanced Energy Materials, 6 (2016) 1600389.
[15] R. Rajagopalan, Z. Zhang, Y. Tang, C. Jia, X. Ji, H. Wang, Energy Storage Materials, 34 (2021) 171-193.
[16] S. Lim, H. Kim, R. Shakoor, Y. Jung, J. Choi, Journal of The Electrochemical Society, 159 (2012) A1393-A1397.
[17] J. Song, S. Park, V. Mathew, J. Gim, S. Kim, J. Jo, S. Kim, M.H. Alfaruqi, J.P. Baboo, I.-H. Kim, S.-J. Song, J. Kim, ACS Applied Materials & Interfaces, 8 (2016) 35235-35242.
[18] X. Ou, X. Liang, C. Yang, H. Dai, F. Zheng, P. Wu, Q. Pan, X. Xiong, M. Liu, Energy Storage Materials, 12 (2018) 153-160.
[19] C.-Y. Huang, Y.-T. Tseng, H.-Y. Lo, J.-K. Chang, W.-W. Wu, Nano Energy, 71 (2020) 104625.
[20] M.T. McDowell, S.W. Lee, J.T. Harris, B.A. Korgel, C. Wang, W.D. Nix, Y. Cui, Nano Letters, 13 (2013) 758-764.
[21] G.-M. Huang, T.-C. Tsai, C.-W. Huang, N. Kumar, T.-Y. Tseng, W.-W. Wu, Nano Energy, 41 (2017) 494-500.
[22] M.D. Graef, M.A. Willard, M.E. McHenry, Z. Yimei, IEEE Transactions on Magnetics, 37 (2001) 2663-2665.
[23] M. Xu, S. Dai, T. Blum, L. Li, X. Pan, Ultramicroscopy, 192 (2018) 1-6.
[24] J.-H. Ho, Y.-H. Ting, J.-Y. Chen, C.-W. Huang, T.-C. Tsai, T.-Y. Lin, C.-Y. Huang, W.-W. Wu, Nano Letters, 18 (2018) 6064-6070.
[25] H.-M. Lu, C.-Y. Huang, G.-M. Huang, K.-C. Lu, W.-W. Wu, Scripta Materialia, 193 (2021) 6-11.
[26] H.-Y. Lo, C.-Y. Yang, G.-M. Huang, C.-Y. Huang, J.-Y. Chen, C.-W. Huang, Y.-H. Chu, W.-W. Wu, Nano Energy, 72 (2020) 104683.
[27] C.-Y. Huang, K.-L. Tai, C.-W. Huang, Y.-T. Tseng, H.-Y. Lo, W.-W. Wu, Scripta Materialia, 177 (2020) 192-197.
[28] Z. Huang, F. Li, C. Jiao, J. Liu, J. Huang, L. Lu, H. Zhang, S. Zhang, Ceramics International, 42 (2016) 6221-6227.
[29] D.S. Su, H.W. Zandbergen, P.C. Tiemeijer, G. Kothleitner, M. Hävecker, C. Hébert, A. Knop-Gericke, B.H. Freitag, F. Hofer, R. Schlögl, Micron, 34 (2003) 235-238.
[30] S. Steinsvik, R. Bugge, J.O.N. GjØNnes, J. TaftØ, T. Norby, Journal of Physics and

Chemistry of Solids, 58 (1997) 969-976.
[31] G. Sun, X. Cao, S. Long, R. Li, P. Jin, Applied Physics Letters, 111 (2017) 053901.
[32] H. Tan, J. Verbeeck, A. Abakumov, G. Van Tendeloo, Ultramicroscopy, 116 (2012) 24-33.
[33] I. Shakhova, M.G. Rozova, D. Burova, D.S. Filimonov, O.A. Drozhzhin, A.M. Abakumov, Journal of Solid State Chemistry, 281 (2020) 121010.
[34] Y. Qi, L. Mu, J. Zhao, Y.-S. Hu, H. Liu, S. Dai, Journal of Materials Chemistry A, 4 (2016) 7178-7184.
[35] A. Shimizu, T. Watanabe, M. Inagaki, Journal of Materials Chemistry, 4 (1994) 1475-1478.
[36] V.M. Pratiwi, H. Purwaningsih, Widyastuti, R. Fajarin, H. Setyawan, IOP Conference Series: Materials Science and Engineering, 202 (2017) 012083.
[37] K. Persson, United States - Materials Project, 2016.
[38] K. Persson, United States - Materials Project, 2014.
[39] A.L. Gavin, G.W. Watson, Physical Chemistry Chemical Physics, 19 (2017) 24636-24646.
[40] G. Li, X. Li, J. Zhao, Q. Zhu, X. Gao, CrystEngComm, 21 (2019) 6978-6984.
[41] C.J. Sun, P. Kung, A. Saxler, H. Ohsato, K. Haritos, M. Razeghi, Journal of Applied Physics, 75 (1994) 3964-3967.
[42] T. Rhimi, G. Leroy, B. Duponchel, K. Khirouni, S. Guermazi, M. Toumi, Ionics, 24 (2018) 3507-3514.
[43] P. Németh, E. Mugnaioli, M. Gemmi, G. Czuppon, A. Demény, C. Spötl, Science Advances, 4 (2018) eaau6178.

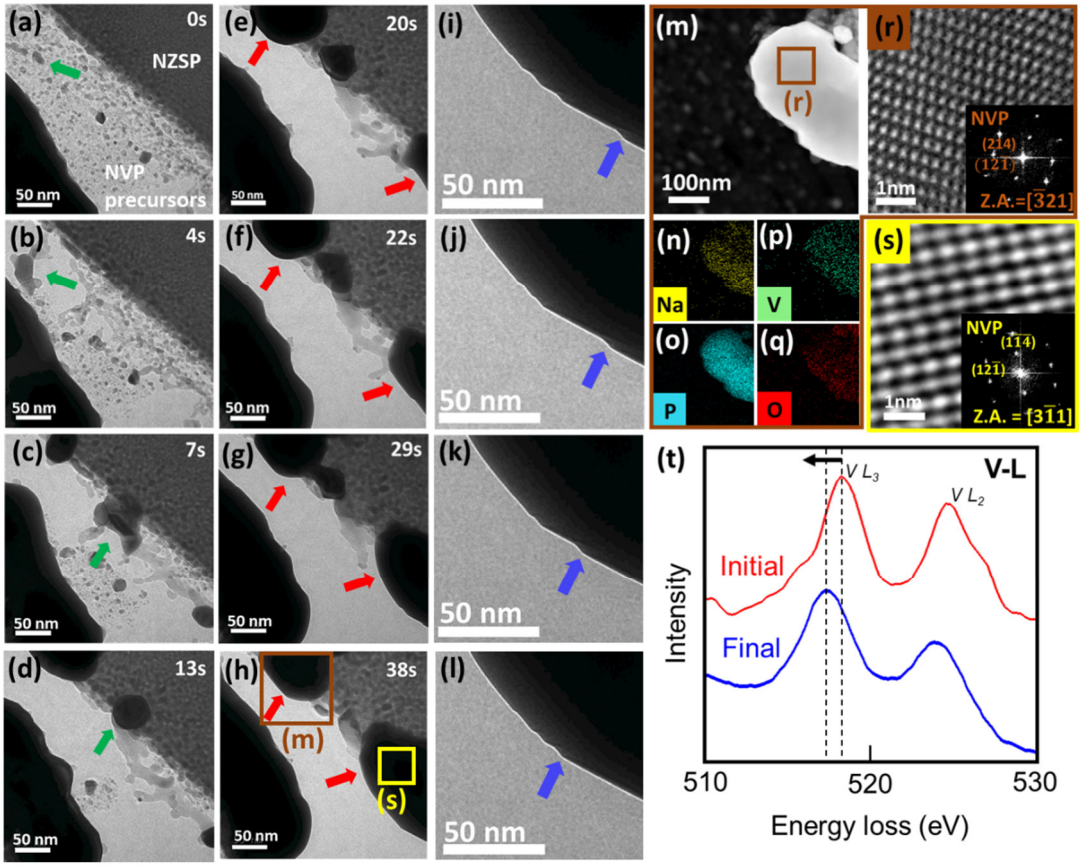

Fig. 1 A series of TEM images, HRTEM images, STEM images, the corresponding FFTs and EDS mapping analysis at low magnification. (a-d) TEM images at low magnification show the aggregation process. (e-h) TEM images at low magnification show the growth process. (i-l) Enlarged TEM images show that NVP trimmed its boundary. (m) Low magnification STEM image of the upper particle formed in (h) after the heating process. (n-q) EDS mapping analysis of Na, V, P and O elements formed in (m). (r) Enlarged HRTEM image and the corresponding FFT of the upper particle formed in (h). (s) Enlarged HRTEM image and the corresponding FFT of the right particle formed in (h). (t) EELS spectra of the initial and final pellets of V (L edges).

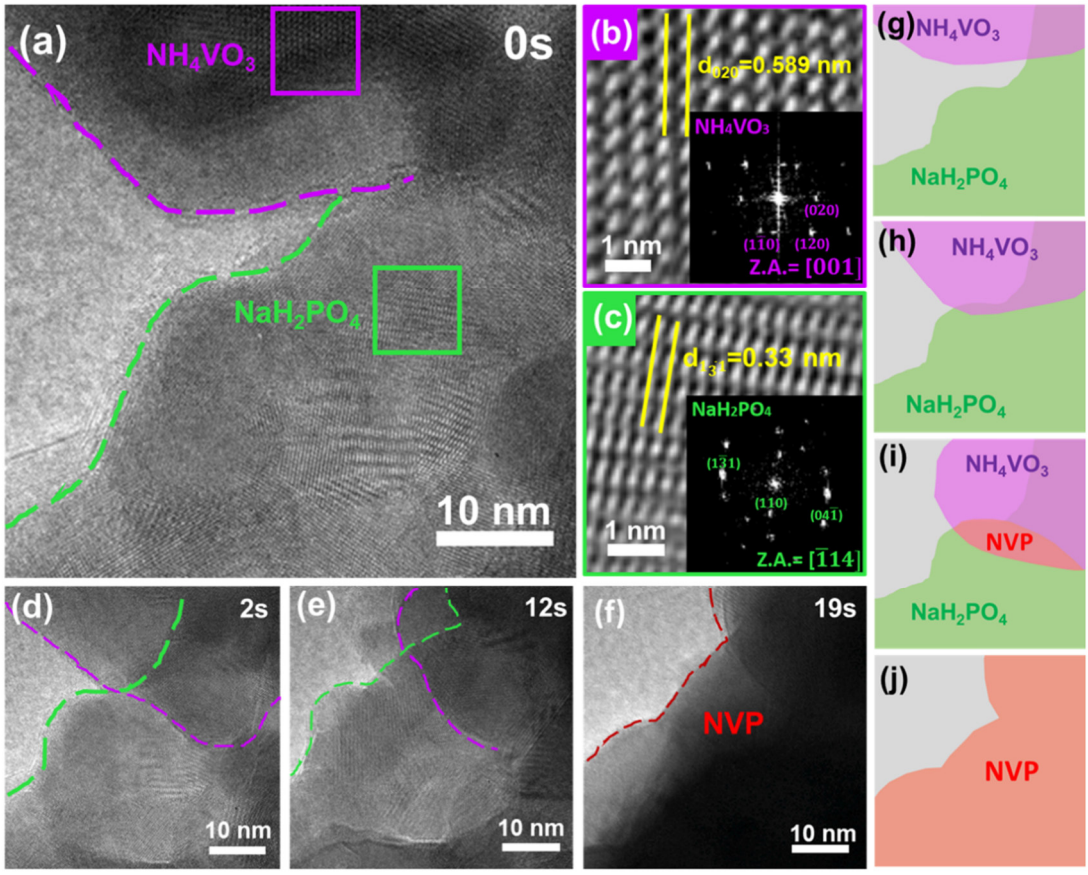

Fig. 2 A series of HRTEM images and the corresponding FFTs showed the aggregation of precursors NaH_2PO_4 and NH_4VO_3. (a) HRTEM image showed the aggregating process of NaH_2PO_4 and NH_4VO_3 at the beginning of movie. (b, c) HRTEM images and the corresponding FFTs of NH_4VO_3 and NaH_2PO_4 formed in (a), respectively. (d-f) HRTEM images showed aggregating process of NaH_2PO_4 and NH_4VO_3. (g-j) Schematic illustration of the aggregation of NaH_2PO_4 and NH_4VO_3.

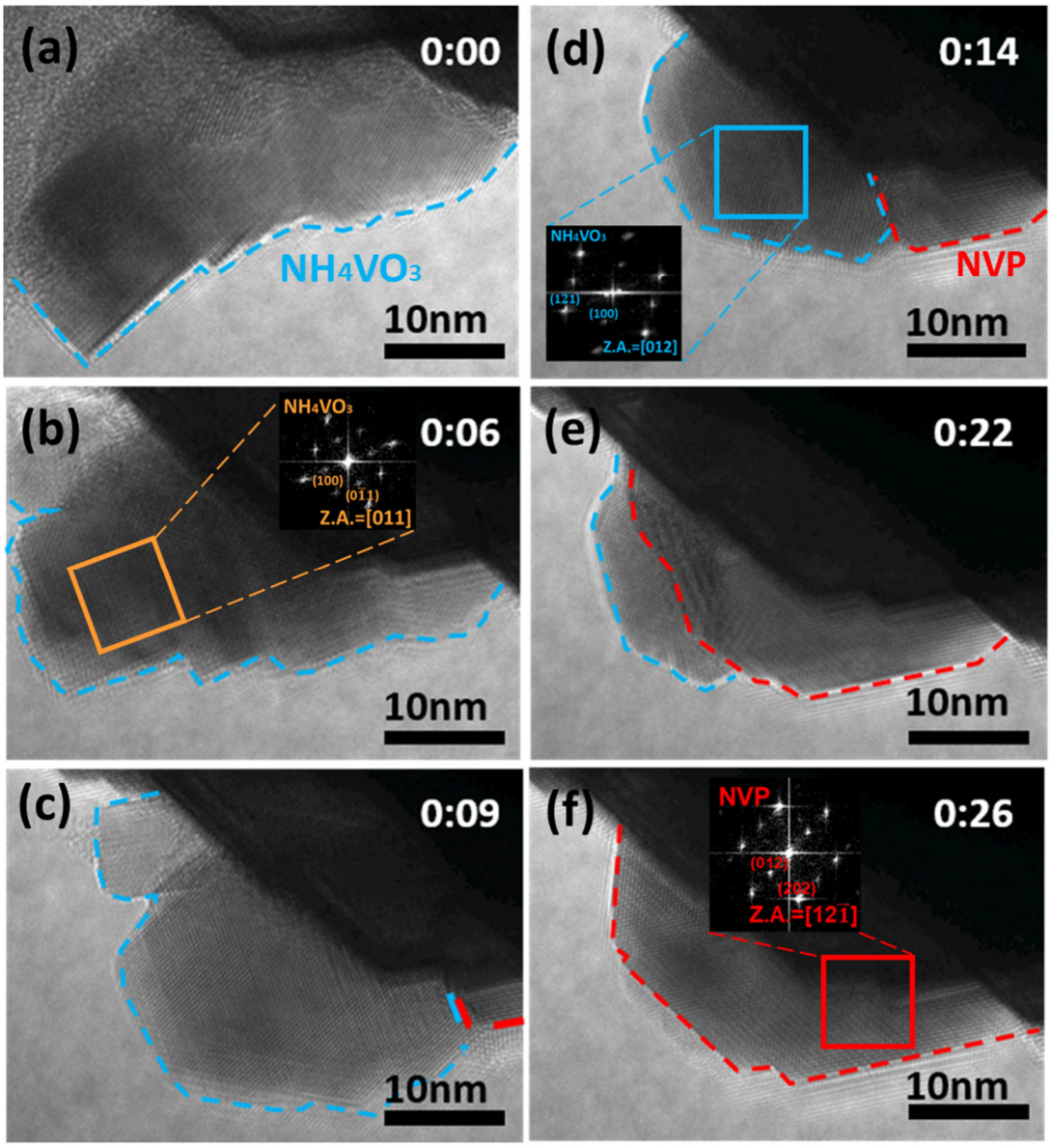

Fig. 3 A series of HRTEM images showed the epitaxial growth process of precursor NH_4VO_3 and NVP. (a-b) HRTEM images of NH_4VO_3 shrank and change direction. (c-f) HRTEM images showed the process of NH_4VO_3 transforming into NVP.

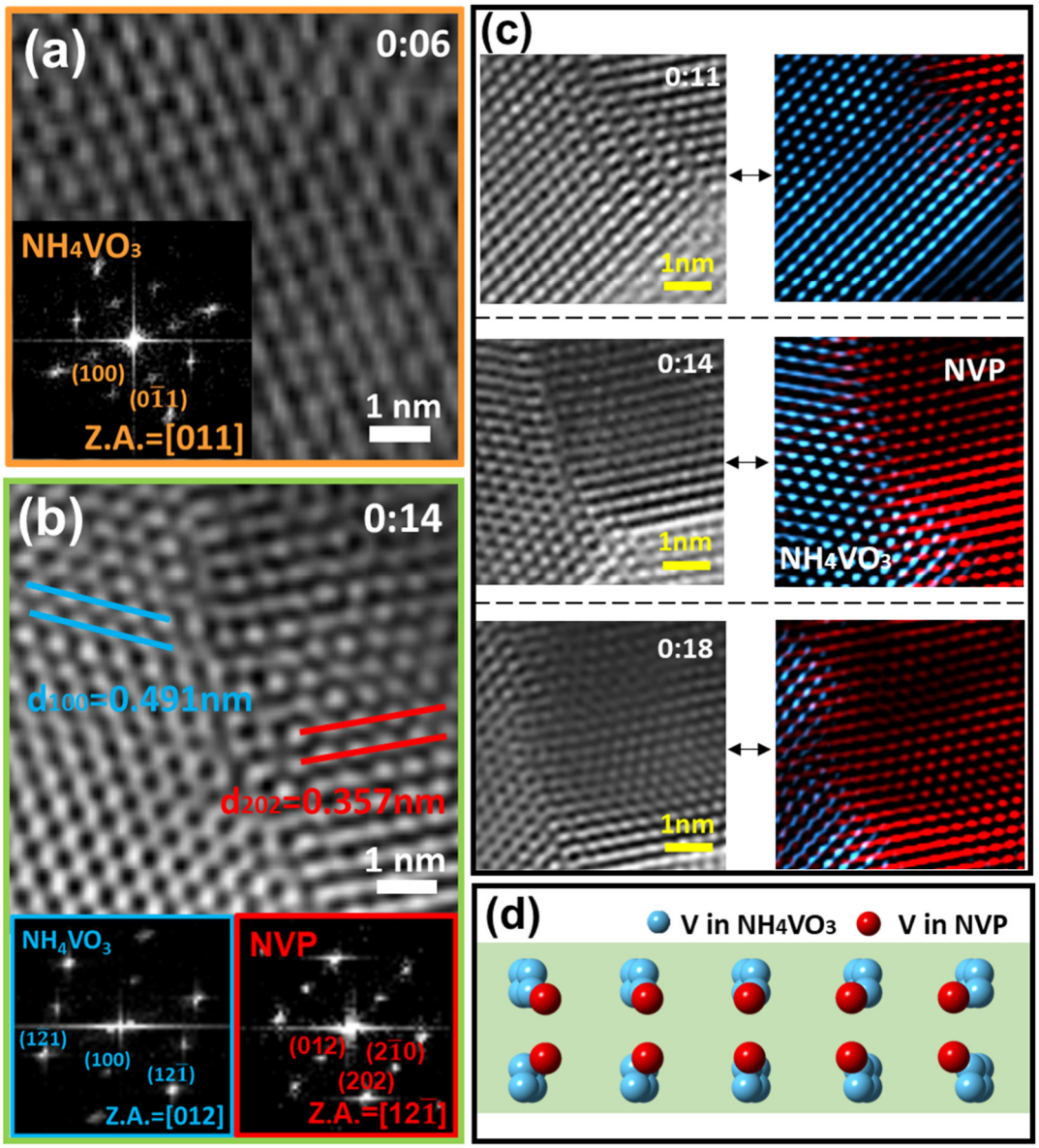

Fig. 4 HRTEM images, corresponding FFTs and schematic illustration at the boundary of NH_4VO_3 and NVP (a) FFTs of NH_4VO_3 formed in Fig. 3b. (b) FFTs of NH_4VO_3 and NVP formed in Fig. 3d. (c) A series of HRTEM images and FFT filtered images showing the phase transformation at the boundary of NH_4VO_3 and NVP. (d) Schematic illustration of the positions of V atoms in NH_4VO_3 and NVP.

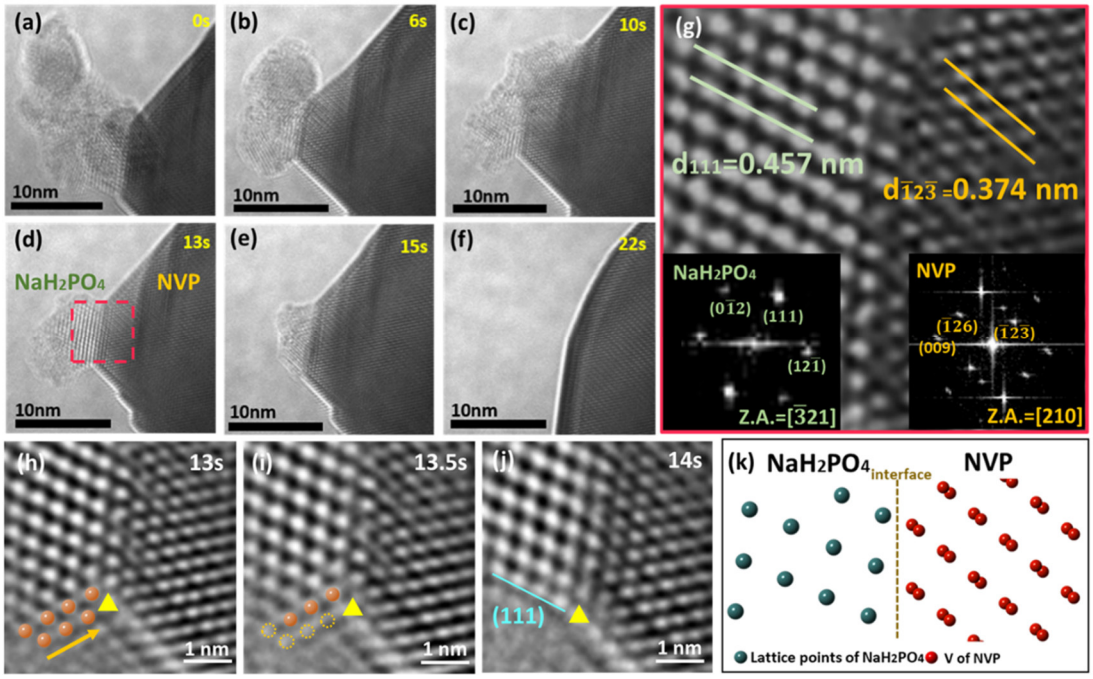

Fig. 5 Epitaxial growth process of precursor NaH_2PO_4 and NVP. (a-f) A series of TEM images showing that NaH_2PO_4 diffused into NVP. (g) HRTEM image and the corresponding FFTs of the NaH_2PO_4 and NVP formed in (d). (h-i) HRTEM images at 13 seconds show the diffusion direction of NaH_2PO_4. (i) HRTEM image at 14 seconds shows the surface facet of NaH_2PO_4. (k) Schematic illustration of the positions of lattice points in NaH_2PO_4 and V atoms in NVP.

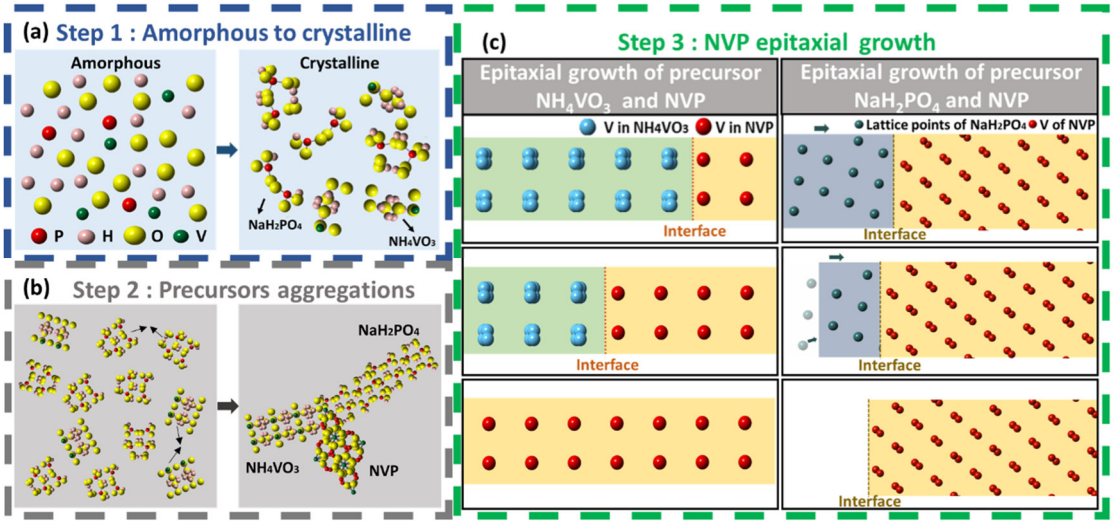

Fig. 6 Schematic illustration showing the mechanism by which NVP formed from precursors. (a-b) Schematics of the crystalline process and aggregate process of NVP precursors. (c) Schematics of the growth process of NVP with precursors NaH_2PO_4 and NH_4VO_3.

Tzu-Hsuan Yu is a Master candidate in Graduate Program of Nanotechnology, Department of Materials Science and Engineering at National Chiao Tung University. Her main research focuses on *in situ* TEM investigation of dynamical changes in nanostructured materials.

Chih-Yang Huang is a Ph.D. candidate in Materials Science and Engineering at National Chiao Tung University. His main research interests are preparation and applications of metal-oxide nanodevices, *in situ* TEM investigation of dynamical changes in nanostructured materials.

Min-Ci Wu is a Ph.D. candidate in Materials Science and Engineering at National Chiao Tung University. Her main research interests are fabrications and applications of memory devices, deposition of metal-oxide thin film, TEM investigation and analysis of nanostructured materials.

Yen-Jung Chen is a candidate for the Bachelor's degree in Materials Science and Engineering at National Chiao Tung University. Her main research interests are applications of metal-oxide RRAM devices, *in situ* TEM investigation of dynamical changes in nanostructured materials.

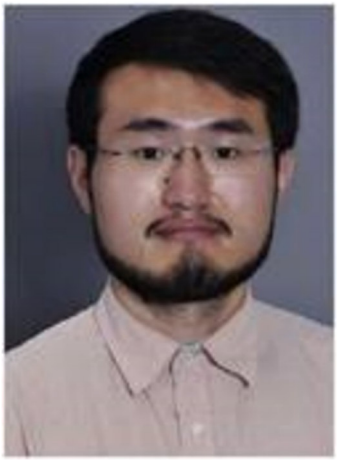

Tu Lan received his B.S. and M.S. degrees from Tsinghua University, Beijing. He did his PhD in RWTH Aachen University in conjunction with his all-solid-state Na battery research works at Forschungszentrum Jülich, institute of energy and climate research, materials synthesis and processing (IEK-1) . He is currently working in Swiss Federal Laboratories for Materials Science and Technology (EMPA), focusing on ZEBRA-type batteries.

Chih-Long Tsai began his scientific career in 1999 as a master student to study on the ferroelectric materials, especially on $(PbMg_{1/3}Nb_{2/3}O_3)_{1-x}(PbTiO_3)_x$. Afterwards, he started his Ph.D. study in Physics Dept. at Montana State University, USA, from 2003

to 2010 to work on high temperature proton conductive SOFC by using $BaZr_xCe_{0.8-x}Y_{0.2}O_3$ as solid electrolyte. After his PhD, he did a short postdoc at CIC enegigune, Spain, to develop inorganic Li-ion conductors for Li batteries in 2011. Since 2012, he joined Forschungszentrum Jülich, IEK-1, to develop all-solid-state Li and Na batteries by using garnet structured Li-ion conductors and NASICON-structured Na-ion conductors.

Jeng-Kuei Chang is currently a Distinguished Professor at National Chiao Tung University. He received his Ph.D. degree from Department of Materials Science and Engineering of National Cheng Kung University. He has worked at Penn State University, Massachusetts Institute of Technology, and Kyushu University as a visiting scholar. Dr. Chang's research focus is on electrochemical energy storage techniques, including Li batteries, Na batteries, Al batteries, supercapacitors, etc.

Prof. Dr. Rüdiger-A. Eichel is full Professor (W3) and chair of Materials and Processes for Electrochemical Energy Conversion and Storage, RWTH Aachen University and Scientific Director Institute of Energy and Climate Research (IEK-9: Fundamental Electrochemistry), Forschungszentrum Jülich. He is also the Founding Director NRW Competence Center Sustainable Electrochemical Process Engineering, the Principle Investigator of the DFG Cluster of Excellence, the Founding Director "Competence Center Sustainable Industrial Electrochemistry" of NRW state in Germany, the Coordinator Helmholtz Cluster of Excellence "Electrochemical CO_2-Valorization" and Flagship-Project for the Transition of the Energy System, the Vice President of the Functional Materials Society.

Prof. Wen-Wei Wu received his Ph.D. degree in Materials Science and Engineering from National Tsing Hua University, 2003. Then he worked as Postdoctoral Fellow (2003–2008) at Materials Science and Engineering, National Tsing Hua University. He joined in Materials Science and Engineering, National Chiao Tung University from 2008. His main research interests are *in situ* TEM investigation of dynamical changes in nanostructured materials, synthesis metal silicide thin films and nanostructures, metallization on Si and Si–Ge alloy, resistive random-access memory, and *in situ* TEM electrochemistry.